Geosci. Model Dev. Discuss., 8, 9103–9146, 2015
www.geosci-model-dev-discuss.net/8/9103/2015/
doi:10.5194/gmdd-8-9103-2015

Geoscientific Model Development Discussions
Open Access
EGU

Inverse transport modeling of volcanic sulfur dioxide emissions using large-scale ensemble simulations

Y. Heng[1,2], L. Hoffmann[1], S. Griessbach[1], T. Rößler[1], and O. Stein[1]

[1]Forschungszentrum Jülich, Jülich Supercomputing Centre (JSC), Jülich, Germany
[2]Forschungszentrum Jülich, Institute of Energy and Climate Research – Tropospheric Research (IEK-8), Jülich, Germany

Received: 3 August 2015 – Accepted: 10 September 2015 – Published: 21 October 2015

Correspondence to: Y. Heng (y.heng@fz-juelich.de)

Published by Copernicus Publications on behalf of the European Geosciences Union.

Abstract

An inverse transport modeling approach based on the concepts of sequential importance resampling and parallel computing is presented to reconstruct altitude-resolved time series of volcanic emissions, which often can not be obtained directly with current measurement techniques. A new inverse modeling and simulation system, which implements the inversion approach with the Lagrangian transport model Massive-Parallel Trajectory Calculations (MPTRAC) is developed to provide reliable transport simulations of volcanic sulfur dioxide (SO_2). In the inverse modeling system MPTRAC is used to perform two types of simulations, i. e., large-scale ensemble simulations for the reconstruction of volcanic emissions and final transport simulations. The transport simulations are based on wind fields of the ERA-Interim meteorological reanalysis of the European Centre for Medium Range Weather Forecasts. The reconstruction of altitude-dependent SO_2 emission time series is also based on Atmospheric Infrared Sounder (AIRS) satellite observations. A case study for the eruption of the Nabro volcano, Eritrea, in June 2011, with complex emission patterns, is considered for method validation. Meteosat Visible and InfraRed Imager (MVIRI) near-real-time imagery data are used to validate the temporal development of the reconstructed emissions. Furthermore, the altitude distributions of the emission time series are compared with top and bottom altitude measurements of aerosol layers obtained by the Cloud–Aerosol Lidar with Orthogonal Polarization (CALIOP) and the Michelson Interferometer for Passive Atmospheric Sounding (MIPAS) satellite instruments. The final transport simulations provide detailed spatial and temporal information on the SO_2 distributions of the Nabro eruption. The SO_2 column densities from the simulations are in good qualitative agreement with the AIRS observations. Our new inverse modeling and simulation system is expected to become a useful tool to also study other volcanic eruption events.

GMDD
8, 9103–9146, 2015

1 Introduction

Observing trace gases and ash released by volcanic eruptions is important for various reasons. Most notably, sulfate aerosols formed by oxidation of SO_2 have significant impact on radiative forcing and are a natural cause for climate variations (Lamb, 1970; Robock, 2000; Solomon et al., 2011). Strong volcanic eruptions inject SO_2 directly into the lower stratosphere. However, more complex transport processes such as the Asian Monsoon circulation have also been investigated (Bourassa et al., 2012; Fromm et al., 2013; Vernier et al., 2013). Further motivation to monitor the dispersion of volcanic emissions is to prevent aircraft from entering potentially dangerous regions, i. e., flight corridors containing high loads of volcanic ash (Casadevall, 1994; Carn et al., 2009; Prata, 2009; Brenot et al., 2014). In practice, the presence of volcanic SO_2 can often be considered as a good proxy for the presence of volcanic ash (Sears et al., 2013).

Satellite instruments are well suited to observe trace gases and aerosols on a global scale and to provide long-term records. Together, volcanic SO_2 and sulfate aerosols provide excellent tracers to study atmospheric transport processes. In order to further improve the quality of available satellite data, e. g., to perform more effectual suppression of interfering background signals, we recently contributed to the development of new detection algorithms for volcanic emissions for European Space Agency (ESA) and National Aeronautics and Space Administration (NASA) satellite experiments (Griessbach et al., 2012, 2014; Hoffmann et al., 2014; Griessbach et al., 2015). However, satellite observations are often limited in temporal and spatial resolution due to their measurement principles. Therefore, atmospheric models are indispensable to study transport processes. In particular, Lagrangian particle dispersion models enable studies of transport and mixing of air masses based on the trajectories of individual air parcels. Widely used models are the Flexible Particle (FLEXPART) model (Stohl et al., 2005), the Hybrid Single-Particle Lagrangian Integrated Trajectory (HYSPLIT) model (Draxler and Hess, 1998), and the Lagrangian Analysis Tool (LAGRANTO) (Wernli and Davies, 1997). Recently, Massive-Parallel Trajectory Calculations (MPTRAC), a new

GMDD
8, 9103–9146, 2015

Lagrangian transport model that is designed for large-scale ensemble simulations on state-of-the-art supercomputers, was developed at the Jülich Supercomputing Centre. A detailed description of MPTRAC and a comparison of the results of transport simulations for volcanic emission events by means of different, freely available meteorological data products, can be found in Hoffmann et al. (2015).

Suitable initializations of the trajectory model, namely the altitude- and time-resolved emission data, are crucial for accurate and reliable simulations of the transport of volcanic SO_2 emissions. However, emissions usually can only be reconstructed indirectly, for instance, by empirical estimates from weather radar measurements (Lacasse et al., 2004), by estimation techniques based on satellite data (Flemming and Inness, 2013; Hoffmann et al., 2015), or by inverse modeling techniques. The work of Flemming and Inness (2013) used satellite retrievals of SO_2 total columns to estimate initial conditions for subsequent SO_2 plume forecasts by applying the Monitoring Atmospheric Composition and Climate (MACC) system (Stein et al., 2012) that is an extension of the 4D-VAR system of the European Centre for Medium Range Weather Forecasts (ECMWF). We refer to previous work (Eckhardt et al., 2008; Stohl et al., 2011; Kristiansen et al., 2012, 2015) on inverse transport modeling techniques in the context of estimating volcanic emissions. Those studies used an analytical inversion algorithm, based on Seibert (2000), for the reconstruction of volcanic ash or SO_2 emission rates. The inversion approach was applied to several case studies such as the 2010 Eyjafjallajökull and the 2014 Kelut eruptions. With respect to the mathematical setting, the estimation task was formulated as a linear inverse problem. To resolve the ill-posedness of this problem, a Tikhonov-type regularization constraint was added. The objective function of the problem quantifies the misfit between model values and observations, but also enforces smoothness of the solution. Several parameters such as the matrix of model sensitivities of observations to source terms and the regularization parameters that tune the smoothness of the solution needed to be provided a priori.

In this paper, we present a new inverse modeling and simulation system that can be used to establish reliable transport simulations for volcanic SO_2 emissions with avail-

GMDD
8, 9103–9146, 2015

able meteorological data and nadir satellite observations. The core of the system, an inversion approach based on the concept of sequential importance resampling (Gordon et al., 1993), is used to reconstruct altitude-dependent time series of volcanic emissions. It assumes that the volcanic SO_2 emissions distribute not only vertically above the location of the volcano (typically from 0 up to 30 km altitude), but also over a period of time (typically for a couple of days). For the numerical computation, a temporal and spatial initialization domain for the volcanic emissions is selected and finely discretized. The fine temporal and spatial discretization of this domain creates a need for large-scale ensemble simulations. However, this setting is well suited for massive-parallel supercomputing architectures. In our case the time- and altitude-dependent volcanic emission rates are estimated efficiently by performing the ensemble simulations in parallel with MPTRAC. A distinct advantage is that the proposed inverse modeling and simulation system does not require an explicit source–receptor relationship and that its flexible design is independent of the choice of Lagrangian particle dispersion model, as long as the forward model can be applied to perform large-scale ensemble simulations.

This paper is organized as follows: We first briefly introduce the Lagrangian transport model MPTRAC, the ERA-Interim meteorological data product, the AIRS satellite observations, and other validation data sets in Sect. 2. In Sect. 3, we present the concept of our new inverse modeling and simulation system, which applies an efficient parallel strategy to perform large-scale ensemble simulations for the reconstruction of volcanic emissions and to establish reliable SO_2 transport simulations. In Sect. 4, we focus on a case study of the Nabro volcano, Eritrea, whose eruption started on 12 June 2011 and lasted several days. Firstly, the reconstructed altitude-resolved time series of volcanic emissions are discussed and validated. Secondly, forward simulation results based on these initial conditions are compared with the AIRS satellite observations. Our conclusions are given in the final section.

GMDD
8, 9103–9146, 2015

2 Transport model and satellite data products

2.1 MPTRAC

In this study we make use of the Lagrangian transport model MPTRAC (Hoffmann et al., 2015) for the forward simulations. MPTRAC calculates the trajectories for large numbers of air parcels to represent the advection of air. The kinematic equation of motion is solved with the explicit midpoint method. Atmospheric diffusion is represented by adding random perturbations to the air parcel trajectories. The physical parameterizations for turbulent diffusion and sub-grid wind fluctuations are based on a Markov model. A hybrid-parallelization scheme based on the Message Passing Interface (MPI) and Open Multi-Processing (OpenMP) is implemented in MPTRAC. The MPI distributed memory parallelization is applied to facilitate ensemble simulations by distributing the ensemble members on the different compute nodes of a supercomputer. Trajectory calculations of an individual ensemble member are distributed over the cores of a compute node by means of the OpenMP shared memory parallelization. This implementation enables rapid forward simulations for ensembles with large numbers of air parcels (typically on the order of 10^2 to 10^4 members per ensemble, with 10^6 to 10^8 air parcels per ensemble member). Moreover, MPTRAC provides efficient means for model output and data visualization. For further details we refer to the work of Hoffmann et al. (2015).

External meteorological data are a prerequisite for the trajectory calculations with MPTRAC. We use the latest global atmospheric reanalysis produced by ECMWF, namely the ERA-Interim data product (Dee et al., 2011). A large variety of 3 hourly surface parameters and 6 hourly upper-air parameters that cover the troposphere and stratosphere are included in the data product. Here, the ERA-Interim standard data on a $1^\circ \times 1^\circ$ longitude-latitude grid are applied. The altitude coverage ranges from the surface to 0.1 hPa with 60 model levels. The vertical resolution in the upper troposphere and lower stratosphere (UT/LS) region varies between 700 and 1200 m. The 6 hourly temporal resolution corresponds to data assimilation cycles at 00:00, 06:00, 12:00,

GMDD
8, 9103–9146, 2015

and 18:00 UTC. A discussion of the analysis increments of the ERA-Interim data, being a figure of merit for the data quality, can be found in Dee et al. (2011). Including a case study for the Nabro eruption, Hoffmann et al. (2015) showed that ERA-Interim data provided the best performance in the Lagrangian transport simulations of volcanic SO_2 with MPTRAC in comparison with three other meteorological data products.

2.2 AIRS

For inversely estimating the volcanic emissions and for validating the simulation results, we use satellite observations of volcanic SO_2 obtained by the AIRS instrument (Aumann et al., 2003; Chahine et al., 2006) aboard NASA's Aqua satellite. Aqua is in a nearly polar, sun-synchronous orbit with Equator-crossing at 01:30 a.m. and 01:30 p.m. local time. Scans in the across-track direction are carried out by means of a rotating mirror. Each scan consists of 90 footprints that correspond to 1765 km distance on the ground surface. Two adjacent scans are separated by 18 km along-track distance. While the AIRS footprint size is 13.5 km × 13.5 km at nadir, it is 41 km × 21.4 km at the scan extremes. Thermal infrared spectra (3.7 to 15.4 µm) for more than 2.9 million footprints are measured by AIRS per day.

Volcanic SO_2 can be detected efficiently from infrared radiance spectra based on brightness temperature differences (BTDs) (e. g., Karagulian et al., 2010; Clarisse et al., 2013). Here we use the BTD identified by Hoffmann et al. (2014) to detect SO_2 from AIRS 7.3 µm radiance measurements and apply their derived SO_2 index (SI) in our study. False detections related to scenes with low brightness temperatures due to deep convective clouds are filtered based on the detection scheme of Hoffmann and Alexander (2010). Hoffmann et al. (2014) demonstrated that their SI is better capable of suppressing background signals than the NASA operational SI and is well suited to trace even low SO_2 concentrations over long time periods. Note that the AIRS data product that is used here provides only horizontally projected values, i. e., no vertical information on the SO_2 distributions is directly available. However, radiative transfer

GMDD
8, 9103–9146, 2015

calculations showed (Hoffmann and Alexander, 2009; Hoffmann et al., 2015) that the SI of Hoffmann et al. (2014) is most sensitive to SO_2 layers at about 8 to 13 km altitude.

2.3 Validation data sets

For validation of the temporal development of the reconstructed emissions, we consider infrared (IR, 11.5 µm) and water-vapor (WV, 6.4 µm) radiance data products from the Meteosat Visible and InfraRed Imager (MVIRI) aboard Eumetsat's Meteosat-7 (Indian Ocean Data Coverage, IODC).[1] MVIRI provides radiance images in three spectral bands from the full earth disc at 5 km × 5 km resolution (sub-satellite point) every 30 min. The MVIRI IR band overlaps with a spectral window region and is used for imaging surface and cloud top temperatures at day and night. The MVIRI WV absorption band is mainly used for determining the amount of water vapour in the upper troposphere. This band is opaque if water vapour is present, but transparent if the air is dry. The WV band can effectively be used to detect volcanic emissions in the upper troposphere because emissions from lower altitudes are blocked by water vapor absorption.

To verify the altitude distribution of the volcanic emissions we consider aerosol measurements from the CALIOP instrument aboard the Cloud–Aerosol Lidar and Infrared Pathfinder Satellite Observations (CALIPSO) satellite (Winker et al., 2010).[2] The spatial resolution of the CALIOP data is 1.67 km (horizontal) × 60 m (vertical) at 8 to 20 km altitude. We also consider aerosol top and bottom altitude measurements from the Michelson Interferometer for Passive Atmospheric Sounding (MIPAS) aboard the Environmental Satellite (Envisat) (Fischer et al., 2008; Griessbach et al., 2015). The spatial sampling of MIPAS in the nominal operation mode during the years 2005 to 2012 was 410 km (horizontal) × 1.5 km (vertical) at 6 to 21 km altitude (Raspollini et al., 2013).

[1] Browse images from http://oiswww.eumetsat.org/IPPS/html/MTP (last access: 10 July 2015).

[2] Browse images at http://www-calipso.larc.nasa.gov/products/lidar/browse_images/production (last access: 10 July 2015).

GMDD
8, 9103–9146, 2015

MIPAS has lower spatial resolution than CALIOP, but it is more sensitive to low aerosol concentrations due to the limb observation geometry.

3 Inverse modeling and simulation system

3.1 Inversion by means of sequential importance resampling

A flow chart of the inverse modeling and simulation system proposed in this paper is shown in Fig. 1. Important system inputs consist of a specification of the time- and altitude-dependent domain for SO_2 emissions, the total number of air parcels for the final forward simulation, the satellite data, and the meteorological data. The Lagrangian transport model MPTRAC is used to perform ensemble forward simulations in a parallel manner. An inversion approach based on the concept of sequential importance resampling (Gordon et al., 1993) in combination with different resampling strategies is proposed to iteratively estimate the volcanic SO_2 emission rates. The emission rates together with the final SO_2 transport simulations are the main output of the system.

We assume that the volcanic SO_2 emissions occur in a time- and altitude-dependent domain $E := [t_0, t_f] \times \Omega$. Here t_0 and t_f denote the initial and final time of possible emissions, and $\Omega := [\lambda_c - 0.5\Delta_\lambda, \lambda_c + 0.5\Delta_\lambda] \times [\phi_c - 0.5\Delta_\phi, \phi_c + 0.5\Delta_\phi] \times [h_l, h_u]$ corresponds to a rectangular column oriented vertically and centered over the volcano. The horizontal coordinates for the volcano are defined by geographic longitude λ_c and geographic latitude ϕ_c. Note that Δ_λ and Δ_ϕ can be varied to control the area of the horizontal cross-section of the column for a particular simulation. h_l and h_u represent the lower and upper boundary of the altitude range used to constrain the emissions. We discretize the domain E along the time axis and the altitude axis with n_t and n_h uniform intervals, respectively. This leads to $N = n_t \cdot n_h$ disjoint subdomains, for which we perform N parallel "unit simulations", correspondingly. Each unit simulation is conducted with an initialization of a given number of air parcels emitted in only one of the disjoint subdomains of E. We refer to the set of all unit simulations at one iteration of

GMDD
8, 9103–9146, 2015

the inversion procedure as an "ensemble simulation". In the iterative inversion procedure, a number of ensemble simulations are usually required to obtain suitable volcanic emission rates.

The N unit simulations at each iteration can be considered as a weighted set of particles, $\{(w_{ij}, s_{ij}), i = 1, \ldots, n_t, j = 1, \ldots, n_h\}$, with s_{ij} and w_{ij} representing the hidden initialization and the relative posterior probabilities of the occurrence of the air parcels for the (i, j)th-unit simulation, respectively. The importance weights w_{ij} have to satisfy the normalization condition $\sum_{i=1}^{n_t} \sum_{j=1}^{n_h} w_{ij} = 1$. By rearranging the importance weights in matrix form, we obtain $\mathbf{W} = (w_{ij})_{i=1,\ldots,n_t;j=1,\ldots,n_h}$ and use this notation in the subsequent sections. This way, the task of reconstructing the altitude-resolved time series of the volcanic emissions mathematically turns into the task of iteratively estimating the importance weight matrix $\mathbf{W}$. Based on the importance weights obtained in the final iteration, the total number of SO_2 air parcels for the possible emissions are redistributed in the entire initialization domain. With the reconstructed emission time series, the final transport simulations are performed.

Our inverse modeling approach is summarized in Algorithm 1. We first discretize the time- and altitude-dependent domain for SO_2 emissions and initialize air parcels in all subdomains with equal probability, i. e., distribute them in time and space uniformly (steps 1–2). Then, as the core part of the system, an iterative procedure (steps 3–6) is used to update the importance weights by performing unit simulations and applying different weight-updating schemes (see details below). The iterative procedure ends when a given termination criterion (step 6) is satisfied. Finally, we use the calculated importance weights to resample the SO_2 air parcels in all subdomains and summarize the information in the entire initialization domain (step 7). With the reconstructed initializations, the final transport simulations are performed (step 8).

GMDD
8, 9103–9146, 2015

3.2 A measure of goodness-of-fit for forward simulations

To evaluate the goodness-of-fit of the forward simulations and to estimate the importance weights w_{ij}, we use the Critical Success Index (CSI) (Donaldson et al., 1975; Schaefer, 1990), adapting the approach presented by Hoffmann et al. (2015). The CSI measures the agreement between the model forecasts and the satellite observations by comparing the spatial extent of the modeled and observed SO_2 plumes over time. Model and observation data are analyzed on a $1^\circ \times 1^\circ$ longitude–latitude grid, accumulated over 12 h time periods. A model forecast is classified as "positive" if the SO_2 amount in a grid box exceeds a certain threshold (for instance, 0.1 % of the assumed total SO_2 mass of all parcels in this case). Likewise, a satellite observation is classified as positive if the mean SI of the AIRS footprints within a grid box exceeds a given threshold. Here we use 2 K, which approximately corresponds to 4 DU (Dobson Units; $1\,\mathrm{DU} = 2.85 \times 10^{-5}\,\mathrm{kg\,m^{-2}}$) in terms of SO_2 column density (Hoffmann et al., 2014).

The CSI is calculated based on event counts of positive and negative model forecasts and satellite observations, respectively. To calculate the CSI, a 2×2 contingency table of the event counts is created first. By denoting the number of positive forecasts with positive observations as c_x, the number of negative forecasts with positive observations as c_y, and the number of positive forecasts with negative observations as c_z, the CSI is defined as

$$\mathrm{CSI} = c_x/(c_x + c_y + c_z). \quad (1)$$

The CSI provides the ratio of successful forecasts (c_x) to the total number of forecasts that were actually made ($c_x + c_z$) or should have been (c_y). Note that the fourth element of the 2×2 contingency table, the number c_w of negative forecasts with negative observations, is not considered in the definition of the CSI. Although c_w is neglected to simply avoid cases of no interest, it should be noted that this causes the CSI to be a biased indicator of forecast skills (Schaefer, 1990).

Since we compare simulation results with satellite observations on a discrete-time finite horizon (12 h time intervals), for each unit simulation the CSI values obtained at

GMDD
8, 9103–9146, 2015

different times t_k can be summarized as a data vector of length n_k. We denote the data vector for the (i,j)th-unit simulation as (CSI_k^{ij}) with $k = 1,\ldots,n_k$ for later use in subsequent sections.

3.3 Iterative update of importance weights and resampling strategies

A straightforward scheme for updating the importance weights w_{ij} is given by

$$w_{ij} = m_{ij} / \sum_{a=1}^{n_t} \sum_{b=1}^{n_h} m_{ab}, \tag{2}$$

where the measure m_{ij} is defined as

$$m_{ij} = \left(\sum_{k=1}^{n_k} \mathrm{CSI}_k^{ij}\right)/n_k. \tag{3}$$

Here, n_k denotes the total number of the time instants of satellite data (12 h intervals) that are used for computing the CSI values. This measure considers an equal weighting of the obtained CSI values of the time series data. As will be shown in Sect. 4, the weight-updating scheme defined by Eqs. (2) and (3), referred to as "mean rule" below, leads to simulations that can capture the basic transport dynamics for the Nabro case study pretty well. However, by definition any non-zero CSI value over the entire observation time period will result in a non-zero importance weight and hence it can not fully exclude cases in which emissions are actually not likely to occur at all. A few representative examples concerning this issue will be shown in Sect. 4.2.

In practice, new SO_2 emissions and already present SO_2 emissions from earlier times are often hard to be distinguished in an initial time period, but they are often more clearly separated at later times. Therefore, an improved measure is suggested

GMDD
8, 9103–9146, 2015

here as

$$\tilde{m}_{ij} = \frac{\sum_{k=1}^{n'_k} \mathrm{CSI}_k^{ij}}{n'_k} \cdot \frac{\sum_{k=n'_k+1}^{n_k} \mathrm{CSI}_k^{ij}}{n_k - n'_k}, \; 1 \le n'_k < n_k, \tag{4}$$

where n'_k is considered as a "split point" for the CSI time series. As will be demonstrated in Sect. 4, the weight-updating scheme defined by Eqs. (2) and (4), referred to as "product rule", can capture not only the basic but also the fine details of the SO_2 transport for the Nabro case study. This is achieved by putting a stronger "and" constraint on the first and second period of the CSI time series. Successful model forecasts in only one of the two time periods will not lead to high importance weights. This way, unlikely local emission patterns can be detected better and excluded, leading to more accurate simulations both globally and locally. Note that the length of the initial time period might be different for each particular volcanic eruption. The split point is chosen at 48 h for the simulations presented here. Nevertheless, the general setting of Eq. (4) allows to control the trade-off between both time periods by tuning n'_k accordingly.

In each iteration of the inversion procedure the measures and corresponding weight-updating schemes based on the CSI data vectors of all unit simulations are evaluated. Furthermore, the numbers of SO_2 air parcels in all subdomains are scaled linearly with the corresponding importance weights. This resampling step redistributes the total SO_2 mass of all air parcels between the subdomains, according to the current importance weights. The iterative procedure ends when the change of importance weight matrices of successive iterations becomes sufficiently small. To quantify the change we use the relative difference d calculated as

$$d(\mathbf{W}^{l+1}, \mathbf{W}^{l}) = \frac{\|\mathbf{W}^{l+1} - \mathbf{W}^{l}\|_F}{\max(\|\mathbf{W}^{l+1}\|_F, \|\mathbf{W}^{l}\|_F)}, l \ge 1, \tag{5}$$

GMDD
8, 9103–9146, 2015

where / denotes the iteration number and $\|\cdot\|_F$ corresponds to the Frobenius norm,

$$\|\mathbf{W}^l\|_F = \sqrt{\sum_{i=1}^{n_t}\sum_{j=1}^{n_h}|w_{ij}^l|^2}. \quad (6)$$

We selected a threshold of 1 % for the relative difference d in our simulations. In the Nabro case study the final importance weights were obtained after 3 iterations.

4 Nabro case study

4.1 Simulation setup

The Nabro is a stratovolcano located at (13°22′ N, 41°42′ E) in Eritrea, Africa. There were no historical eruptions recorded before June 2011. However, at about 20:30 UTC on 12 June 2011, a series of earthquakes resulted in a strong volcanic eruption. Volcanic activity lasted over 5 days and various plume altitudes occurred. Clarisse et al. (2012) reported a total SO_2 mass of approximately 1.5×10^9 kg in the UT/LS region based on measurements by the Infrared Atmospheric Sounding Interferometer (IASI). As a significant amount of ash was emitted, some regional flights had to be cancelled.[3] Due to the complexities of its emission patterns and transport processes related to the Asian monsoon circulation, we consider the Nabro eruption as an excellent example to validate our inverse modeling approach.

As described in Sect. 3, we here consider different types of simulations, i. e., unit simulations used for the reconstruction of the altitude-dependent time series of the Nabro SO_2 emissions and final forward simulations based on the estimated emission data. Regarding the unit simulations we assume that the SO_2 emissions occurred in the vicinity of the Nabro volcano within a horizontal area of 1° × 1° at 0 to 30 km altitude

[3] See http://www.bbc.com/news/world-africa-13778171 (last access: 22 June 2015).

GMDD
8, 9103–9146, 2015

between 12 June 2011, 12:00 UTC and 18 June 2011, 00:00 UTC. For the numerical discretization of the emission domain, a time step of 1 h and an altitude step of 250 m are applied. This discretization leads to 132 × 120 = 15 840 subdomains. For the reconstruction of the SO_2 emission rates we use the AIRS satellite data between 13 June 2011, 00:00 UTC and 23 June 2011, 00:00 UTC. In each iteration of the inversion procedure, 15 840 unit simulations for the subdomains were carried out. These large-scale ensemble simulations were performed in parallel on the Jülich Research on Petaflop Architectures (JuRoPA) supercomputer[4].

For the final forward simulations, starting on 12 June 2011, 12:00 UTC and running for 15 days, a total number of 2 million air parcels is considered. AIRS satellite data between 13 June 2011, 00:00 UTC and 28 June 2011, 00:00 UTC are considered to validate these simulation results. In Sect. 4.6 we compare final forward simulations obtained with different weight-updating schemes. The first scheme assumes that the SO_2 emissions have equal probability of occurrence in the initialization domain. Namely, equal importance weights, $w_{ij} = 1/15\,840$, are considered for initializations in all 15 840 subdomains. This type of simulation does not require any measurement information such as the satellite observations. Although such an assumption is unrealistic in practice, it serves as a good initial condition for our inversion procedure to estimate the final importance weights with the other weight-updating schemes. By applying the mean rule and the product rule, the iterative inversion procedure reconstructs more realistic time- and altitude-dependent volcanic SO_2 emission rates than the equal probability scheme.

4.2 Examples of unit simulations

In order to illustrate the basic idea behind the weight-updating schemes in the frame of the proposed inversion approach we first study individual unit simulations. Figures 2 to 4 show the results of the CSI analysis for three representative examples. Since the

[4]See http://www.fz-juelich.de/ias/jsc/juropa (last access: 22 June 2015).

GMDD
8, 9103–9146, 2015

AIRS satellite data used here lack vertical information, only horizontally projected simulation results are used for this analysis. As mentioned earlier, the analysis is performed on a $1^\circ \times 1^\circ$ longitude-latitude grid.

Based on these examples, the unit simulations can be classified into three categories. In the first category, we consider the cases in which the assigned initialization in the specific subdomain yields SO_2 air parcel trajectories that follow the satellite observations well. As an example, Fig. 2 shows the unit simulation with an initialization of emissions at 13 June 2011, 00:00 UTC ±30 min and at (16.5 ± 0.125) km altitude. This simulation shows excellent agreement with parts of the satellite observations over the entire simulation time period. This indicates that SO_2 emissions most likely occurred in the corresponding temporal and spatial subdomain.

In the second category, we consider the cases where model forecasts quickly mismatch the satellite observations. As an example, Fig. 3 shows a model forecast related to emissions released at the same time as in the first example, but at (29 ± 0.125) km altitude. Figure 3 illustrates that the forecasts agree with the satellite observations only shortly after the volcanic eruption. After 12 h the SO_2 air parcels were already transported westwards, not agreeing with the satellite observations. Hence, this indicates that SO_2 emissions were not likely to occur in this temporal and spatial subdomain.

In the third category, successful model forecasts can be found for a longer time period compared with second category. The example presented in Fig. 4, with air parcels released at the same time but at (20 ± 0.125) km altitude, shows agreement between the model forecast and the satellite observations for about 2 days. However, the SO_2 air parcels were transported westwards and are not agreeing with the satellite observations at later times. Also in this temporal and spatial subdomain SO_2 emissions were not likely to occur.

In summary, a good inverse modeling strategy should be able to identify and separate all cases in the aforementioned three different categories and yield suitable importance weights. As will be shown in the subsequent sections, both the mean rule and the product rule work well for the cases in the first category. They can therefore capture

GMDD
8, 9103–9146, 2015

the basic transport dynamics. However, for less realistic situations in the second and third category the application of the mean rule still yields small importance weights. The product rule can be used to exclude these unrealistic cases and yield proper importance weights by choosing a suitable split point of the obtained CSI time series. As will be shown in Sect. 4.6, it is therefore considered as a superior strategy, both qualitatively and quantitatively.

4.3 Reconstruction of volcanic SO_2 emissions

Suitable initializations are necessary in order to perform reliable final forward simulations. For this purpose we estimate the time- and altitude-dependent volcanic SO_2 emissions with the iterative inversion approach outlined in Sect. 3. The time- and altitude-resolved emission rates are estimated based on the different weight-updating schemes. The simple equal-probability resampling strategy (first guess) assumes an equal weight of $w_{ij} = 1/15\,840$ that leads to an equal emission rate of approximately $0.1052\,\mathrm{kg\,m^{-1}\,s^{-1}}$ in the entire initialization domain. However, note that such an assumption is in general not very realistic, even by posing further time- and altitude-constraints, because volcanic eruptions often change over time significantly and emissions are also not uniformly distributed with altitude.

Figure 5 shows the temporally and spatially resolved SO_2 emission rates reconstructed by applying the mean rule and the product rule, respectively. The application of the mean rule results in temporally and spatially broader areas with smaller emission rates (Fig. 5, top) up to about $1.5\,\mathrm{kg\,m^{-1}\,s^{-1}}$. As shown in the figure, some unlikely cases of local emissions mentioned in Sect. 4.2, e. g., at altitudes above 20 km or below 5 km, are not excluded. Since the total amount of emitted SO_2 is fixed, the emission rates of likely local emissions (e. g., on 13 June 2011, 00:00 UTC at altitude 16.5 km) are underestimated.

In contrast, the application of the product rule emphasizes the more likely cases and excludes unlikely cases (Fig. 5, bottom). Its maximum emission rate is about

GMDD
8, 9103–9146, 2015

6 times larger than that of the mean rule. In particular, the peak emission rates on 13 June 2011, 00:00 UTC, 14 June 2011, 15:00 UTC, and 16 June 2011, 10:00 UTC are approximately 9.28 $kg\,m^{-1}\,s^{-1}$, 0.57 $kg\,m^{-1}\,s^{-1}$, and 0.70 $kg\,m^{-1}\,s^{-1}$, respectively. The corresponding peak emission rates estimated by the mean rule are approximately 1.50 $kg\,m^{-1}\,s^{-1}$, 0.56 $kg\,m^{-1}\,s^{-1}$, and 0.42 $kg\,m^{-1}\,s^{-1}$, which are likely to be underestimated.

Our results qualitatively agree with the emission data reconstructed by the backward-trajectory approach presented by Hoffmann et al. (2015, Figs. 6 and 14). The maximum emission rates obtained by the backward-trajectory approach are in between the maximum values obtained with the mean rule and the product rule weight-updating schemes used here. Even closer agreement with the backward-trajectory approach might be achieved by tuning the split point of the product rule accordingly. A sensitivity study for this important tuning parameter will be presented in Sect. 4.5.

Finally, Fig. 6 shows the reconstructed emission rates integrated over time and altitude, respectively. As found earlier, the maximum emission rates for the main eruption on 13 June obtained by the product rule are much higher (up to a factor of 2 for the integrated values) than those obtained by the mean rule. However, this is compensated by lower emission rates by the product rule from 14 to 17 June. Considering the altitude distribution, Fig. 6 (bottom) reveals, especially for the product rule, that most SO_2 emissions occurred at 10 to 12 and 15 to 17 km altitude. We find that the altitude distribution is less constrained for the mean rule than for the product rule.

4.4 Validation of emission time series

In Fig. 7 we show time series information for the Nabro eruption that are obtained from MVIRI IR and WV measurements aboard Meteosat-7 (IODC). The satellite imagery indicates that the strongest eruptions occurred between 13 June 2011, 00:00 and 12:00 UTC. A series of smaller emission events until 16 June 2011, 15:00 UTC were also observed. In particular, there were two short-time periods of strong eruptions on 14 and and 16 June 2011, respectively. The emission time series derived

GMDD
8, 9103–9146, 2015

with our inverse modeling approach are in good temporal agreement with the MVIRI observations.

Injection altitudes of the Nabro eruption have been discussed recently, mostly based on different satellite measurements (Bourassa et al., 2012; Fromm et al., 2013; Vernier et al., 2013; Fromm et al., 2014). The first CALIOP measurements found the initial plume at 11–15.5 km over Pakistan and at 15–16.5 km over Iran on 15 June. Plumes were measured at 18–19 km and 8.5 –11.5 km over Egypt, at 16–17.5 km over Turkey, at 8.5–11 km over the Arabian Peninsula, at 16–17 km over Iran, and at 14–16.2 km over China on 16 June. MIPAS detected the aerosol resulting from Nabro eruption at 12–16.5 km over Israel on 14 June. The aerosol layers nearest to the Nabro were measured at 11–16.5 km on 15 June. They reached 16–18.5 km on 16 June and 12–15.5 km on 17 June. The altitudes measured by CALIOP and MIPAS agree within their uncertainties.

The relatively inhomogeneous plume altitudes can also be seen in our reconstructed emission time series, indicating multiple segregated eruption events. The first eruption on 13 June was the strongest and mainly reached altitudes of 15–17 km. This is confirmed by CALIOP and MIPAS measurements that even found aerosol up to 19 km (in low concentrations). On 14 June the second eruption injected the volcanic emissions into altitudes of 9–13 km. At these altitudes aerosols were also measured by CALIOP and MIPAS. Starting from the afternoon of 15 June to 16 June, the injection altitude increased again to about 17 km, although emission rates are lower than for the first and second eruption. This is confirmed by MIPAS measurements over Egypt on 17 June reaching up to 17.5 km. Fromm et al. (2013) and Vernier et al. (2013) reported that the initial eruption on 13 June reached altitudes between 15 and 19 km, which is in good agreement with our reconstructed plume. Fromm et al. (2014) reported an injection altitude of 17.4 km for the third eruption on 16 June, which is less than 1 km above our reconstructed injection altitude. This initial validation with the different satellite observations indicates that our reconstructed emission time series are reliable.

GMDD
8, 9103–9146, 2015

4.5 Sensitivity analysis for the weight-updating schemes

In this section, we first discuss the effect of different choices of the parameter n_k for the mean rule weight-updating scheme. As discussed in Sect. 3.2, n_k denotes the total number of discrete-time intervals used for the CSI analysis. It directly corresponds to the choice of the final time step of the satellite data. For the reference simulations we have chosen 23 June 2011, 00:00 UTC as the final time, corresponding to $n_k = 21$. Figure 8 (top) displays a contour plot of the importance weights for the reference case. Figure 8 (middle and bottom) shows the absolute differences with respect to other final times. By choosing 22 June 2011, 00:00 UTC ($n_k = 19$) and 24 June 2011, 00:00 UTC ($n_k = 23$) as the final times, the relative differences of the importance weights are about 9.5 and 10 %, respectively. The choice of 22 June 2011, 12:00 UTC ($n_k = 20$) and 23 June 2011, 12:00 UTC ($n_k = 22$) as final time lead to smaller relative differences, about 7.2 and 6.2 %, respectively (not shown). Based on a visual inspection, the aforementioned different importance weights all show rather similar results in the final forward simulations.

For the product rule, we performed a sensitivity analysis with n_k corresponding to the reference date (23 June 2011, 00:00 UTC), but we choose five different split points n'_k, corresponding to 24 h, 36 h, 48 h, 60 h, and 72 h after the beginning of the simulation (13 June 2011, 00:00 UTC). Considering 48 h as the reference case, the choice of the other split points lead to 23.1, 11.3, 8.7, and 13.7 % relative differences of the importance weights. Except in the case of 24 h, which is too short to constrain the time and altitude distribution of the SO_2 emissions properly, the other three cases lead to weights close to the reference and similar results in the final forward simulations. Figure 9 illustrates the results of this sensitivity test. It shows the importance weights for the reference split point (48 h) and the absolute differences of the importance weights for split points at 36 and 60 h, respectively.

GMDD
8, 9103–9146, 2015

4.6 Final forward simulations

We performed the final forward simulations for the Nabro case study with the initializations obtained in Sect. 4.3. Figure 10 shows the corresponding CSI time series based on 12 h time intervals, obtained by applying the equal-probability strategy, the mean rule, and the product rule, respectively. In all cases, the largest CSI values are found at the beginning of the simulations, followed by an overall decrease towards the end of the simulation. The equal-probability strategy yields a maximum CSI value of 32.3 % and a mean CSI value of 8.1 %. The inversions that apply the mean rule and the product rule both lead to higher CSI values. The mean rule yields better simulation results than the equal-probability strategy, because it takes into account the temporal variations and inhomogeneous plume altitudes of the volcanic eruption. Its maximum and mean CSI values are 41.2 and 16.6 %, respectively. The application of the product rule provides the best simulation results of all three cases. Its maximum and mean CSI values are 52.4 and 21.4 %, respectively.

Figures 11 to 15 compare the simulation results with AIRS satellite observations for selected time steps. SO_2 column densities from the model are presented on a $0.5^\circ \times 0.5^\circ$ longitude-latitude grid. The AIRS SO_2 index during corresponding 12 h time periods is presented on the measurement grid of the instrument. In the case of the equal-probability strategy, unrealistic transport of air parcels westward of the Nabro is found. Accordingly, the estimated SO_2 column densities for realistic pathways are significantly lower. In the case of the mean rule, more realistic forecasts of the basic SO_2 transport patterns are obtained. The simulation results are qualitatively closer to the satellite observations both in time and space. However, unrealistic westward transport of SO_2 is still recognizable. The product rule clearly yields the most reliable simulation results of the three cases. It most successfully excludes unlikely local emission patterns.

GMDD
8, 9103–9146, 2015

5 Conclusions and outlook

In this paper, we presented an inversion approach based on the concept of sequential importance resampling for the reconstruction of volcanic emission rates from infrared nadir satellite observations. Based on the proposed inversion approach, a new inverse modeling and simulation system, implemented with the Lagrangian transport model MPTRAC, has been developed to enable efficient and reliable transport simulations of volcanic SO_2 emissions. Our solution is in general independent of the choice of forward transport model and well suited for massive-parallel supercomputing architectures.

Together with the equal-probability assumption, two weight-updating schemes, referred to as the mean rule and product rule have been proposed for the reconstruction of emission data. Considering the Nabro eruption in June 2011 as a case study, we assessed the reconstructed emission time series by comparing them with Meteosat-7 (IODC) imagery to validate the temporal development and with CALIOP and MIPAS satellite observations to confirm the injection altitudes. Simulation results based on the initializations reconstructed by different weight-updating schemes have been compared, in particular, to demonstrate the advantages of the product rule. The simulation results for the Nabro case study show good agreement with the AIRS satellite observations in terms of SO_2 horizontal distributions. The simulation results show that the inverse modeling system successfully identified the complex volcanic emission pattern of the Nabro eruption, and helped to further reveal the complex transport processes through the Asian monsoon circulation.

Some topics were explicitly excluded from this paper, but may be investigated in future work, including the extension of the current approach towards near-real-time forecasting and the development of an adaptive strategy for discretizing the initialization domain. An adaptive strategy is expected to reduce the computational effort and to provide better resolution in areas of the initialization domain where there is large variability. This way, we would expect more precise importance weights estimated for the most likely cases of local emission and hence more accurate simulation results with

GMDD
8, 9103–9146, 2015

better local details in a quantitative manner. Further research shall also be devoted to the testing of the proposed MPTRAC-based inverse modeling and simulation system for other case studies of volcanic eruptions and its capacity for forecasting.

Code and data availability

The current release of the MPTRAC model can be downloaded from the model web site at http://www.fz-juelich.de/ias/jsc/mptrac. The code version used in this study can be obtained by contacting the corresponding author. The time- and altitude-dependent emission time series obtained with the different weight-updating schemes (Fig. 5) are provided as an electronic supplement to this paper. This allows our results to be reproduced and extended in further work, for instance by performing simulations with other transport models.

The Supplement related to this article is available online at doi:10.5194/gmdd-8-9103-2015-supplement.

Acknowledgements. AIRS data products were obtained from the NASA Goddard Earth Sciences Data Information and Services Center (GES DISC). ERA-Interim data were obtained from the European Centre for Medium-Range Weather Forecasts (ECMWF). The authors gratefully acknowledge the computing time granted on the supercomputer JuRoPA at the Jülich Supercomputing Centre (JSC).

The article processing charges for this open-access publication were covered by a Research Centre of the Helmholtz Association.

References

Aumann, H. H., Chahine, M. T., Gautier, C., Goldberg, M. D., Kalnay, E., McMillin, L. M., Revercomb, H., Rosenkranz, P. W., Smith, W. L., Staelin, D. H., Strow, L. L., and Susskind, J.: AIRS/AMSU/HSB on the Aqua Mission: design, science objective, data products, and processing systems, IEEE T. Geosci. Remote, 41, 253–264, 2003. 9109

Bourassa, A. E., Robock, A., Randel, W. J., Deshler, T., Rieger, L. A., Lloyd, N. D., Llewellyn, E. J. T., and Degenstein, D. A.: Large volcanic aerosol load in the stratosphere linked to Asian Monsoon transport, Science, 337, 78–81, 2012. 9105, 9121

Brenot, H., Theys, N., Clarisse, L., van Geffen, J., van Gent, J., Van Roozendael, M., van der A, R., Hurtmans, D., Coheur, P.-F., Clerbaux, C., Valks, P., Hedelt, P., Prata, F., Rasson, O., Sievers, K., and Zehner, C.: Support to Aviation Control Service (SACS): an online service for near-real-time satellite monitoring of volcanic plumes, Nat. Hazards Earth Syst. Sci., 14, 1099–1123, doi:10.5194/nhess-14-1099-2014, 2014. 9105

Carn, S. A., Krueger, A. J., Krotkov, N. A., Yang, K., and Evans, K.: Tracking volcanic sulfur dioxide clouds for aviation hazard mitigation, Nat. Hazards, 51, 325–343, 2009. 9105

Casadevall, T. J.: The 1989-1990 eruption of Redoubt Volcano, Alaska: impacts on aircraft operations, J. Volcanol. Geoth. Res., 62, 301–316, 1994. 9105

Chahine, M. T., Pagano, T. S., Aumann, H. H., Atlas, R., Barnet, C., Blaisdell, J., Chen, L., Divakarla, M., Fetzer, E. J., Goldberg, M., Gautier, C., Granger, S., Hannon, S., Irion, F. W., Kakar, R., Kalnay, E., Lambrigtsen, B. H., Lee, S., Marshall, J. L., McMillan, W. W., McMillin, L., Olsen, E. T., Revercomb, H., Rosenkranz, P., Smith, W. L., Staelin, D., Strow, L. L., Susskind, J., Tobin, D., Wolf, W., and Zhou, L.: AIRS: improving weather forecasting and providing new data on greenhouse gases, B. Am. Meteorol. Soc., 87, 911–926, 2006. 9109

Clarisse, L., Hurtmans, D., Clerbaux, C., Hadji-Lazaro, J., Ngadi, Y., and Coheur, P.-F.: Retrieval of sulphur dioxide from the infrared atmospheric sounding interferometer (IASI), Atmos. Meas. Tech., 5, 581–594, doi:10.5194/amt-5-581-2012, 2012. 9116

Clarisse, L., Coheur, P.-F., Prata, F., Hadji-Lazaro, J., Hurtmans, D., and Clerbaux, C.: A unified approach to infrared aerosol remote sensing and type specification, Atmos. Chem. Phys., 13, 2195–2221, doi:10.5194/acp-13-2195-2013, 2013. 9109

Dee, D. P., Uppala, S. M., Simmons, A. J., Berrisford, P., Poli, P., Kobayashi, S., Andrae, U., Balmaseda, M. A., Balsamo, G., Bauer, P., Bechtold, P., Beljaars, A. C. M., van de Berg, L.,

GMDD
8, 9103–9146, 2015

Bidlot, J., Bormann, N., Delsol, C., Dragani, R., Fuentes, M., Geer, A. J., Haimberger, L., Healy, S. B., Hersbach, H., Hólm, E. V., Isaksen, L., Kãllberg, P., Köhler, M., Matricardi, M., McNally, A. P., Monge-Sanz, B. M., Morcrette, J.-J., Park, B.-K., Peubey, C., de Rosnay, P., Tavolato, C., Thépaut, J.-N., and Vitart, F.: The ERA-Interim reanalysis: configuration and performance of the data assimilation system, Q. J. Roy. Meteor. Soc., 137, 553–597, 2011. 9108, 9109

Donaldson, R., Dyer, R. M., and Kraus, M. J.: Objective evaluator of techniques for predicting severe weather events, B. Am. Meteor. Soc., 56, 755–755, 1975. 9113

Draxler, R. R. and Hess, G. D.: An overview of the HYSPLIT_4 modeling system of trajectories, dispersion, and deposition, Aust. Meteorol. Mag., 47, 295–308, 1998. 9105

Eckhardt, S., Prata, A. J., Seibert, P., Stebel, K., and Stohl, A.: Estimation of the vertical profile of sulfur dioxide injection into the atmosphere by a volcanic eruption using satellite column measurements and inverse transport modeling, Atmos. Chem. Phys., 8, 3881–3897, doi:10.5194/acp-8-3881-2008, 2008. 9106

Fischer, H., Birk, M., Blom, C., Carli, B., Carlotti, M., von Clarmann, T., Delbouille, L., Dudhia, A., Ehhalt, D., Endemann, M., Flaud, J. M., Gessner, R., Kleinert, A., Koopman, R., Langen, J., López-Puertas, M., Mosner, P., Nett, H., Oelhaf, H., Perron, G., Remedios, J., Ridolfi, M., Stiller, G., and Zander, R.: MIPAS: an instrument for atmospheric and climate research, Atmos. Chem. Phys., 8, 2151–2188, doi:10.5194/acp-8-2151-2008, 2008. 9110

Flemming, J. and Inness, A.: Volcanic sulfur dioxide plume forecasts based on UV satellite retrievals for the 2011 Grímsvötn and the 2010 Eyjafjallajökull eruption, J. Geophys. Res., 118, 10–172, 2013. 9106

Fromm, M., Nedoluha, G., and Charvát, Z.: Comment on “Large Volcanic Aerosol Load in the Stratosphere Linked to Asian Monsoon Transport”, Science, 339, 647-c, doi:10.1126/science.1228605, 2013. 9105, 9121

Fromm, M., Kablick III, G., Nedoluha, G., Carboni, E., Grainger, R., Campbell, J., and Lewis, J.: Correcting the record of volcanic stratospheric aerosol impact: Nabro and Sarychev Peak, J. Geophys. Res., 119, 10343–10364, 2014. 9121

Gordon, N. J., Salmond, D. J., and Smith, A. F. M.: Novel approach to nonlinear/non-Gaussian Bayesian state estimation, Radar and Signal Processing, IEE Proceedings F, 140, 107–113, 1993. 9107, 9111

GMDD
8, 9103–9146, 2015

Griessbach, S., Hoffmann, L., von Hobe, M., Müller, R., Spang, R., and Riese, M.: A six-year record of volcanic ash detection with Envisat MIPAS, in: Proceedings of ESA ATMOS 2012, European Space Agency, ESA Special Publication SP-708 (CD-ROM), 2012. 9105

Griessbach, S., Hoffmann, L., Spang, R., and Riese, M.: Volcanic ash detection with infrared limb sounding: MIPAS observations and radiative transfer simulations, Atmos. Meas. Tech., 7, 1487–1507, doi:10.5194/amt-7-1487-2014, 2014. 9105

Griessbach, S., Hoffmann, L., Spang, R., von Hobe, M., Müller, R., and Riese, M.: Infrared limb emission measurements of aerosol in the troposphere and stratosphere, Atmos. Meas. Tech. Discuss., 8, 4379–4412, doi:10.5194/amtd-8-4379-2015, 2015. 9105, 9110

Hoffmann, L. and Alexander, M. J.: Retrieval of stratospheric temperatures from Atmospheric Infrared Sounder radiance measurements for gravity wave studies, J. Geophys. Res., 114, D07105, doi:10.1029/2008JD011241, 2009. 9110

Hoffmann, L. and Alexander, M. J.: Occurrence frequency of convective gravity waves during the North American thunderstorm season, J. Geophys. Res., 115, D20111, doi:10.1029/2010JD014401, 2010. 9109

Hoffmann, L., Griessbach, S., and Meyer, C. I.: Volcanic emissions from AIRS observations: detection methods, case study, and statistical analysis, Proc. SPIE, 9242, 924214–924214-8, doi:10.1117/12.2066326, 2014. 9105, 9109, 9110, 9113

Hoffmann, L., Rößler, T., Griessbach, S., Heng, Y., and Stein, O.: Lagrangian transport simulations of volcanic sulfur dioxide emissions: impact of meteorological data products, J. Geophys. Res., submitted, 2015. 9106, 9108, 9109, 9110, 9113, 9120

Karagulian, F., Clarisse, L., Clerbaux, C., Prata, A. J., Hurtmans, D., and Coheur, P. F.: Detection of volcanic SO_2, ash, and H_2SO_4 using the Infrared Atmospheric Sounding Interferometer (IASI), J. Geophys. Res., 115, D00L02, doi:10.1029/2009JD012786, 2010. 9109

Kristiansen, N. I., Stohl, A., Prata, A. J., Bukowiecki, N., Dacre, H., Eckhardt, S., Henne, S., Hort, M. C., Johnson, B. T., Marenco, F., Neininger, B., Reitebuch, O., Seibert, P., Thomson, D. J., Webster, H. N., and Weinzierl, B.: Performance assessment of a volcanic ash transport model mini-ensemble used for inverse modeling of the 2010 Eyjafjallajökull eruption, J. Geophys. Res., 117, D00U11, doi:10.1029/2011JD016844, 2012. 9106

Kristiansen, N. I., Prata, A. J., Stohl, A., and Carn, S. A.: Stratospheric volcanic ash emissions from the 13 February 2014 Kelut eruption, Geophys. Res. Lett., 42, 588–596, 2015. 9106

GMDD
8, 9103–9146, 2015

Lacasse, C., Karlsdóttir, S., Larsen, G., Soosalu, H., Rose, W., and Ernst, G.: Weather radar observations of the Hekla 2000 eruption cloud, Iceland, B. Volcanol., 66, 457–473, 2004. 9106

Lamb, H. H.: Volcanic dust in the atmosphere, with a chronology and assessment of its meteorological significance, Philos. T. Roy. Soc. A, 266, 425–533, 1970. 9105

Prata, A. J.: Satellite detection of hazardous volcanic clouds and the risk to global air traffic, Nat. Hazards, 51, 303–324, 2009. 9105

Raspollini, P., Carli, B., Carlotti, M., Ceccherini, S., Dehn, A., Dinelli, B. M., Dudhia, A., Flaud, J.-M., López-Puertas, M., Niro, F., Remedios, J. J., Ridolfi, M., Sembhi, H., Sgheri, L., and von Clarmann, T.: Ten years of MIPAS measurements with ESA Level 2 processor V6 – Part 1: Retrieval algorithm and diagnostics of the products, Atmos. Meas. Tech., 6, 2419–2439, doi:10.5194/amt-6-2419-2013, 2013. 9110

Robock, A.: Volcanic eruptions and climate, Rev. Geophys., 38, 191–219, 2000. 9105

Schaefer, J. T.: The critical success index as an indicator of warning skill, Weather Forecast., 5, 570–575, 1990. 9113

Sears, T. M., Thomas, G. E., Carboni, E. A., Smith, A. J., and Grainger, R. G.: SO_2 as a possible proxy for volcanic ash in aviation hazard avoidance, J. Geophys. Res., 118, 5698–5709, 2013. 9105

Seibert, P.: Inverse modelling of sulfur emissions in Europe based on trajectories, in: Volume 114 of Geophysical Monograph, American Geophysical Union, Washington DC, USA, 147–154, 2000. 9106

Solomon, S., Daniel, J. S., Neely, R., Vernier, J.-P., Dutton, E. G., and Thomason, L. W.: The persistently variable "background" stratospheric aerosol layer and global climate change, Science, 333, 866–870, 2011. 9105

Stein, O., Flemming, J., Inness, A., Kaiser, J. W., and Schultz, M. G.: Global reactive gases forecasts and reanalysis in the MACC project, J. Integr. Environ. Sci., 9, 57–70, 2012. 9106

Stohl, A., Forster, C., Frank, A., Seibert, P., and Wotawa, G.: Technical note: The Lagrangian particle dispersion model FLEXPART version 6.2, Atmos. Chem. Phys., 5, 2461–2474, doi:10.5194/acp-5-2461-2005, 2005. 9105

Stohl, A., Prata, A. J., Eckhardt, S., Clarisse, L., Durant, A., Henne, S., Kristiansen, N. I., Minikin, A., Schumann, U., Seibert, P., Stebel, K., Thomas, H. E., Thorsteinsson, T., Tørseth, K., and Weinzierl, B.: Determination of time- and height-resolved volcanic ash emis-

GMDD
8, 9103–9146, 2015

sions and their use for quantitative ash dispersion modeling: the 2010 Eyjafjallajökull eruption, Atmos. Chem. Phys., 11, 4333–4351, doi:10.5194/acp-11-4333-2011, 2011. 9106
Vernier, J.-P., Thomason, L. W., Fairlie, T. D., Minnis, P., Palikonda, R., and Bedka, K. M.: Comment on "Large Volcanic Aerosol Load in the Stratosphere Linked to Asian Monsoon Transport", Science, 339, 647-d, doi:10.1126/science.1227817, 2013. 9105, 9121
Wernli, H. and Davies, H. C.: A Lagrangian-based analysis of extratropical cyclones, I: The method and some applications, Q. J. Roy. Meteor. Soc., 123, 467–489, 1997. 9105
Winker, D. M., Pelon, J., Coakley, J. A., Ackerman, S. A., Charlson, R. J., Colarco, P. R., Flamant, P., Fu, Q., Hoff, R. M., Kittaka, C., Kubar, T. L., Le Treut, H., McCormick, M. P., Mégie, G., Poole, L., Powell, K., Trepte, C., Vaughan, M. A., and Wielicki, B. A.: The CALIPSO Mission: a global 3D view of aerosols and clouds, B. Am. Meteorol. Soc., 91, 1211–1229, 2010. 9110

GMDD
8, 9103–9146, 2015

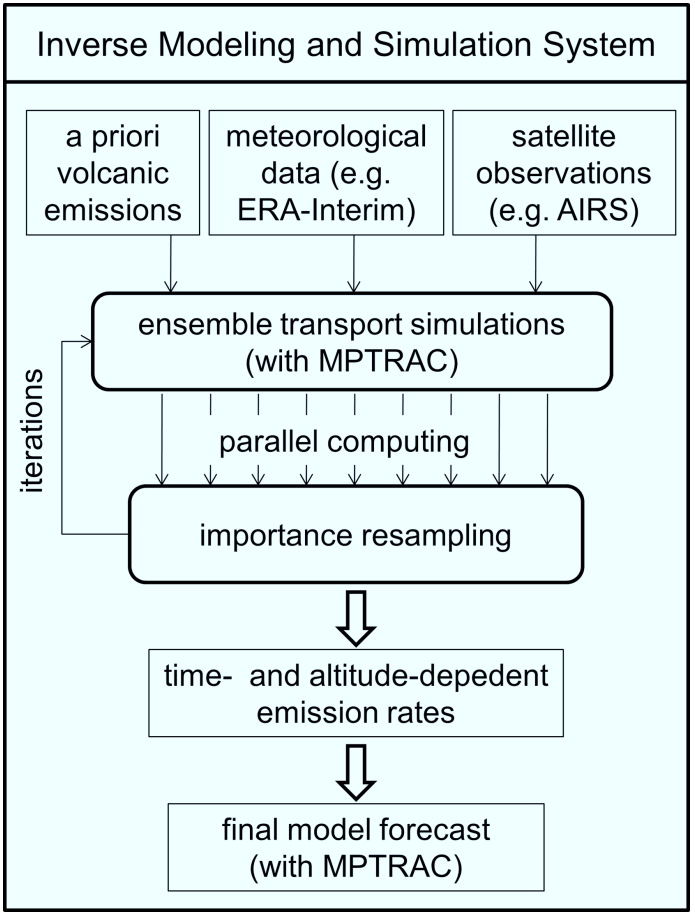

Figure 1. Flow chart of the proposed inverse modeling and simulation system to infer volcanic SO_2 emissions rates and to perform transport simulations.

GMDD
8, 9103–9146, 2015

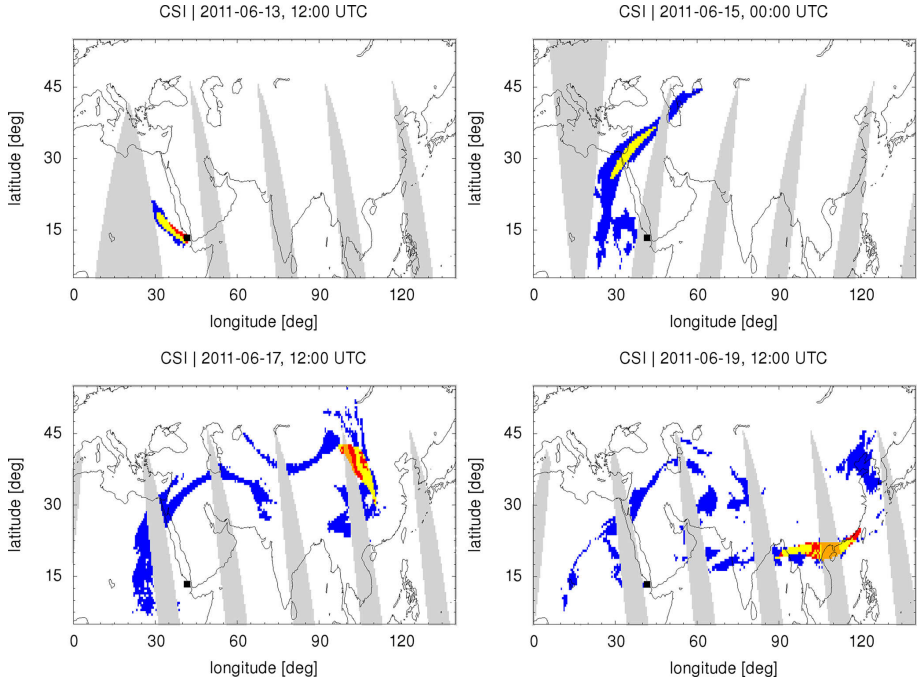

Figure 2. Unit simulation for the Nabro case study with air parcels initialized around 13 June, 00:00 UTC and 16.5 km altitude. The CSI analysis is performed on a $1^{\circ} \times 1^{\circ}$ longitude-latitude grid. Gray color indicates missing satellite data. Orange color corresponds to positive model forecasts, but lack of satellite data. Yellow color indicates positive forecasts and positive satellite observations. Blue color corresponds to negative forecasts with positive observations. Red color corresponds to positive forecasts with negative observations. The black square shows the location of the Nabro volcano.

GMDD
8, 9103–9146, 2015

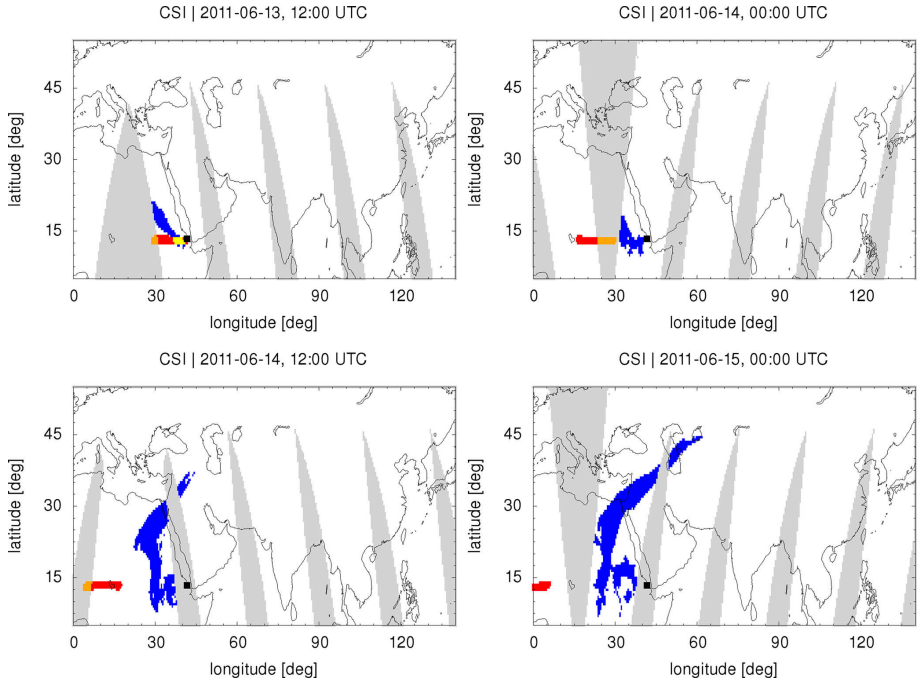

Figure 3. Same as Fig. 2, but for a unit simulation initialized at 29 km altitude. This simulation almost immediately disagrees with the satellite observations. Note that the time steps are partly different from those shown in Fig. 2.

GMDD
8, 9103–9146, 2015

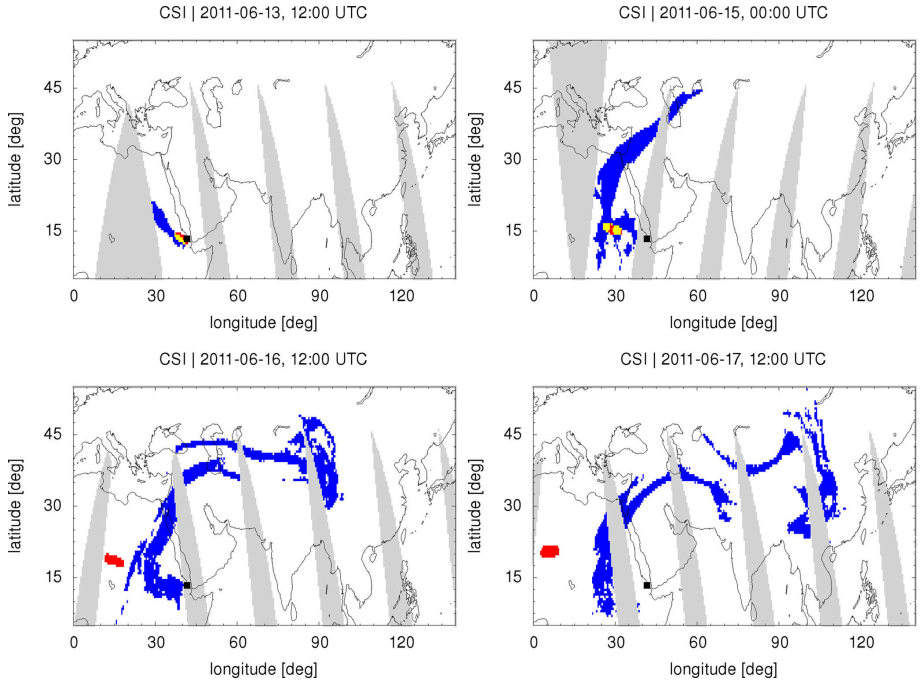

Figure 4. Same as Fig. 2, but for a unit simulation initialized at 20 km altitude. This simulations agrees with the satellite observations for about 48 h, but disagrees at later times. Note that the time steps are partly different from those shown in Figs. 2 and 3.

GMDD
8, 9103–9146, 2015

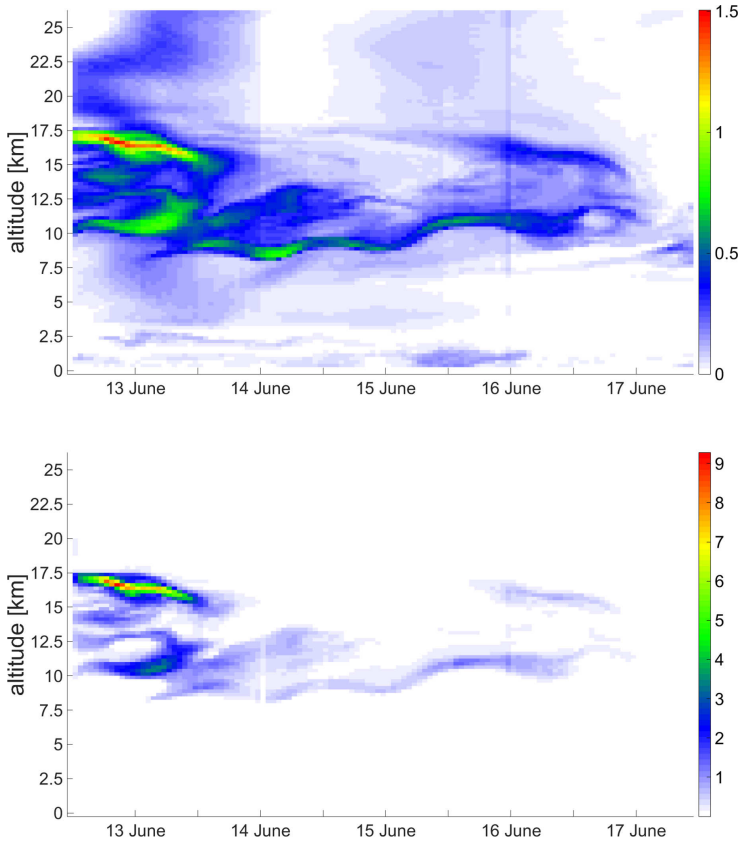

Figure 5. Reconstructed SO_2 emission rates ($kg\,m^{-1}\,s^{-1}$) for the Nabro eruption in June 2011. Emission rates were obtained by applying the mean rule (top) and the product rule (bottom) weight-updating schemes of the proposed inversion approach (see text for details).

GMDD
8, 9103–9146, 2015

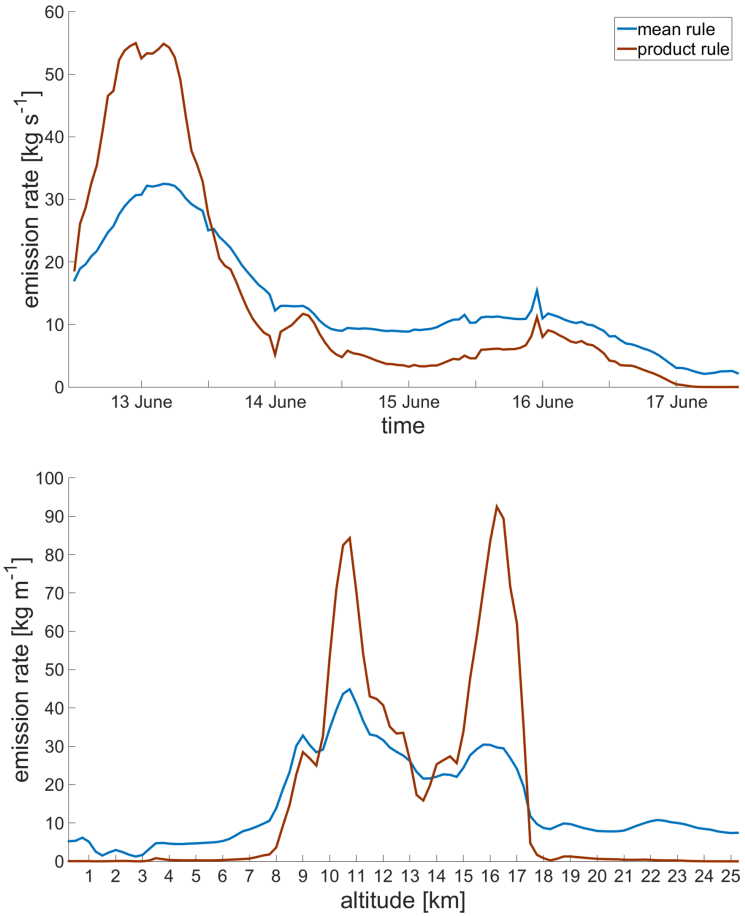

Figure 6. Comparison of reconstructed emission rates integrated over altitude (top) and time (bottom) for the mean rule and the product rule weight-updating schemes.

GMDD
8, 9103–9146, 2015

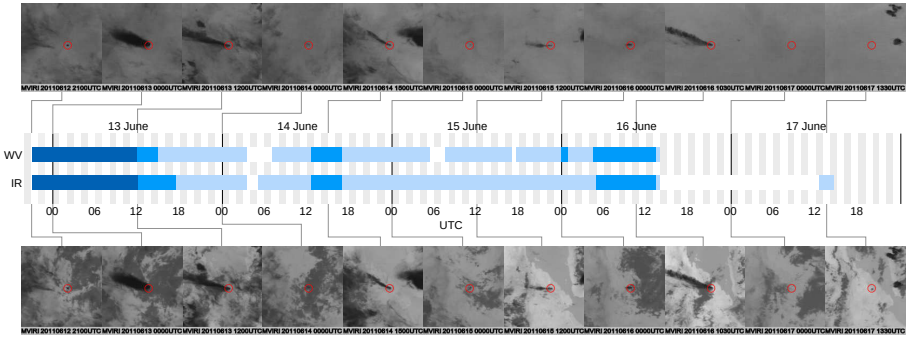

Figure 7. Time line of the 2011 Nabro eruption based on MVIRI IR and WV measurements from Meteosat-7 (IODC). The satellite images were used to roughly estimate the strength of the volcanic activity (white = none, light blue = low level, blue = medium level, dark blue = high level).

GMDD
8, 9103–9146, 2015

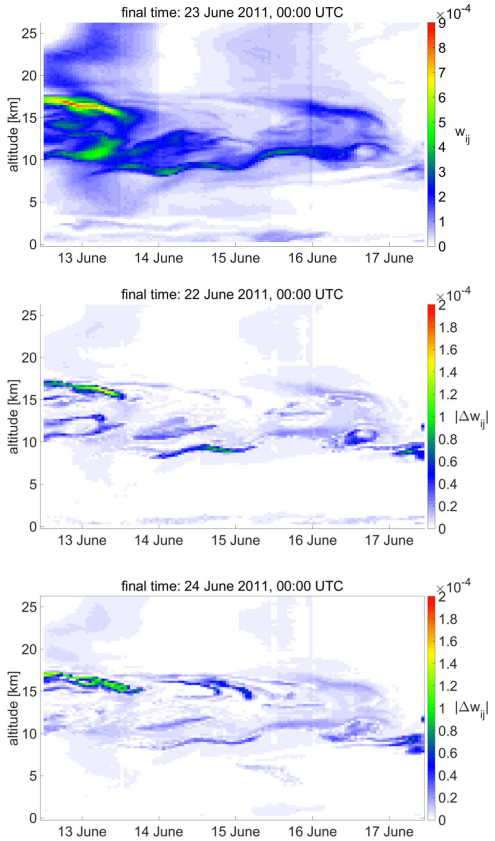

Figure 8. Sensitivity analysis for the mean rule parameter n_k: estimated importance weights w_{ij} for choosing 23 June, 00:00 UTC as the final time of used satellite data (top); absolute differences of estimated importance weights $|\Delta w_{ij}|$ for choosing 23 June, 00:00 UTC as the final time and those for choosing 22 June, 00:00 UTC (middle) and 24 June, 00:00 UTC (bottom) as final time.

GMDD
8, 9103–9146, 2015

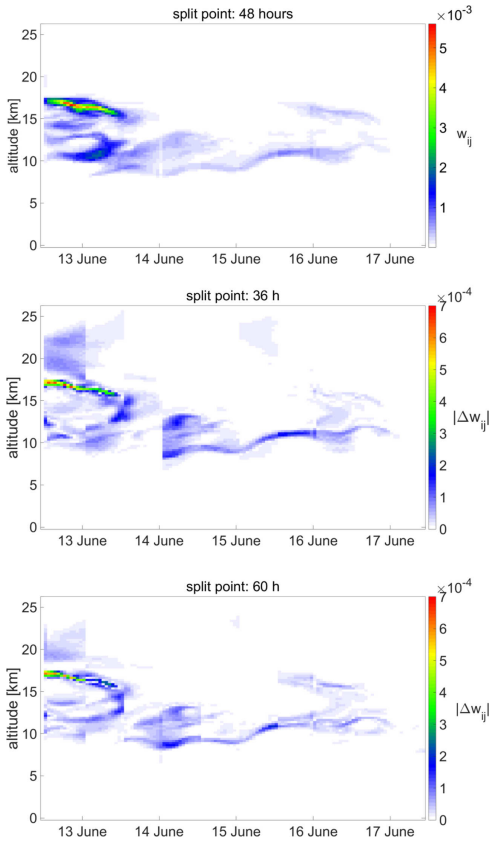

Figure 9. Sensitivity analysis for the product rule parameter n'_k: estimated importance weights w_{ij} for choosing 23 June 00:00 as the final time of used satellite data and 48 h as the split point (top); absolute differences of estimated importance weights $|\Delta w_{ij}|$ for choosing 48 h as the split point and those for choosing 36 h (middle) and 60 h (bottom) as split point.

GMDD
8, 9103–9146, 2015

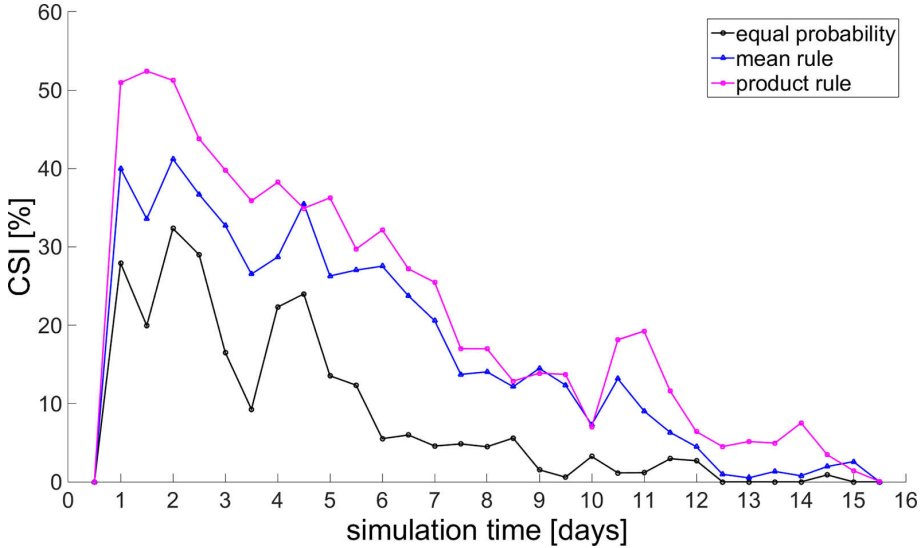

Figure 10. Comparison of the Critical Success Index (CSI) during 12 h time intervals obtained by applying the equal-probability strategy, the mean rule, and the product rule.

GMDD
8, 9103–9146, 2015

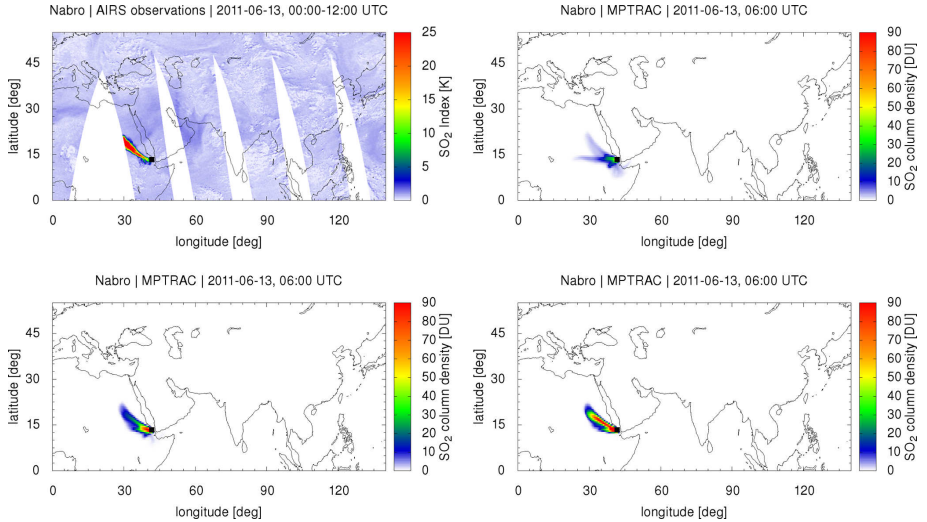

Figure 11. Comparison of AIRS satellite observations (top, left) and MPTRAC simulation results on 13 June 2011, 06:00 UTC based on the equal-probability strategy (top, right), the mean rule (bottom, left), and the product rule (bottom, right).

GMDD
8, 9103–9146, 2015

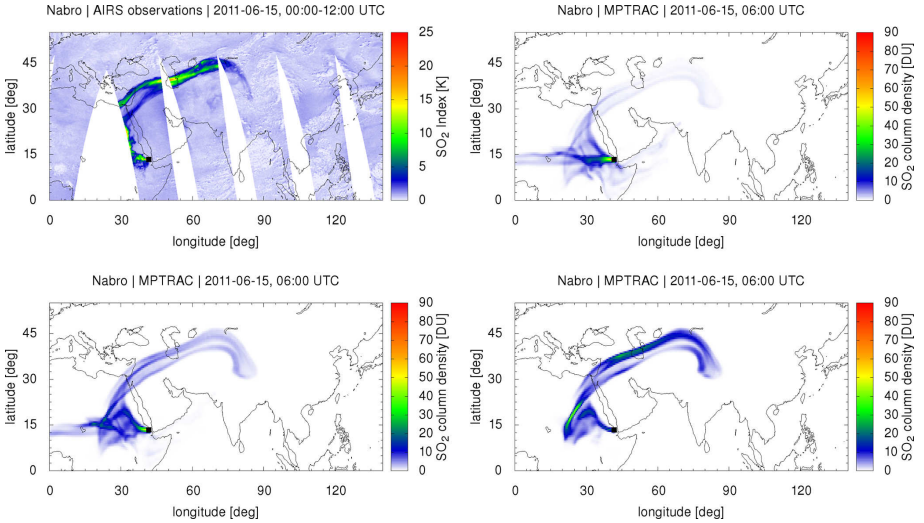

Figure 12. Same as Fig. 11, but for 15 June 2011, 06:00 UTC.

GMDD
8, 9103–9146, 2015

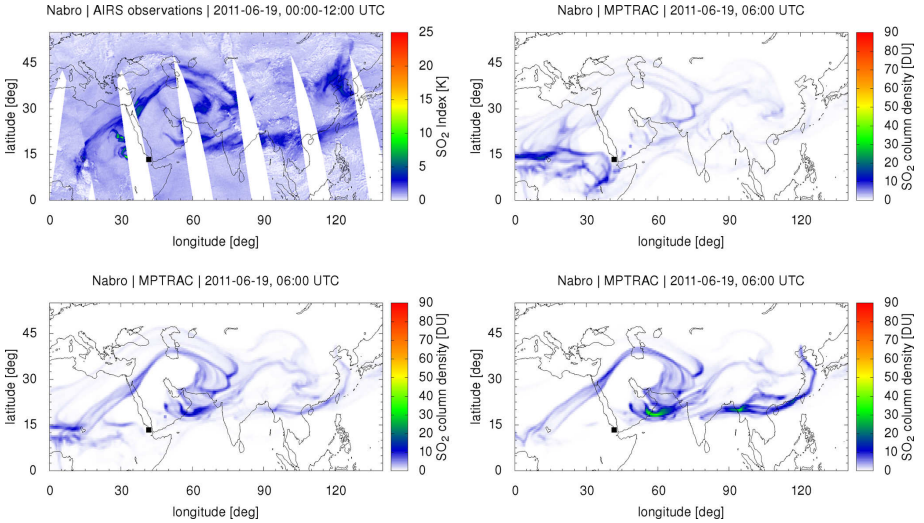

Figure 13. Same as Fig. 11, but for 19 June 2011, 06:00 UTC.

GMDD
8, 9103–9146, 2015

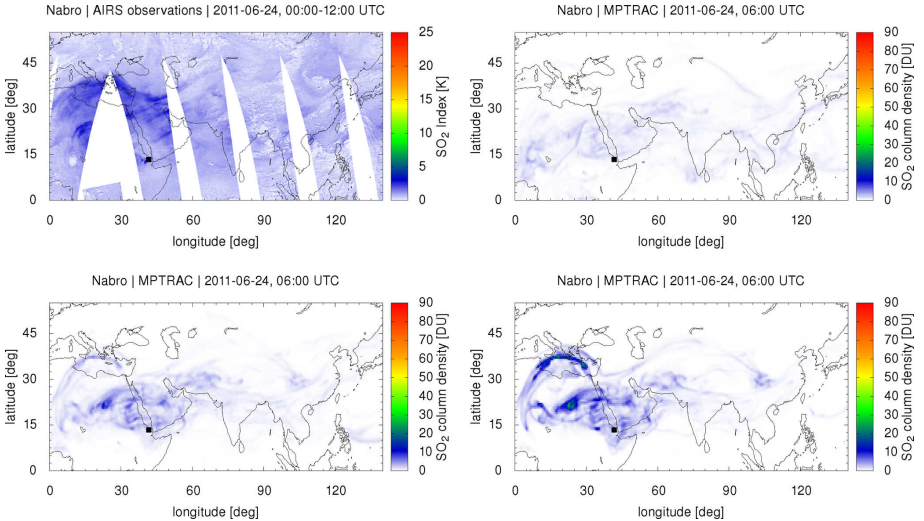

Figure 14. Same as Fig. 11, but for 24 June 2011, 06:00 UTC.

GMDD
8, 9103–9146, 2015

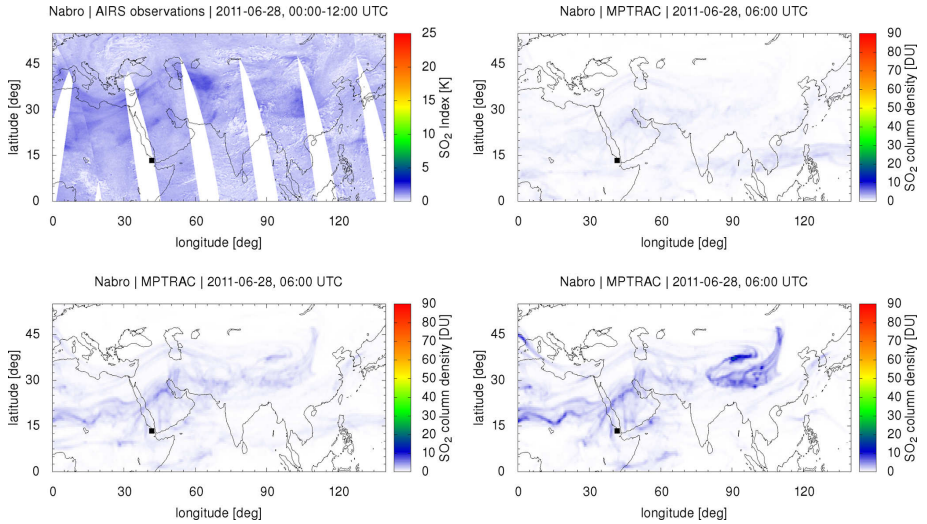

Figure 15. Same as Fig. 11, but for 28 June 2011, 06:00 UTC.

GMDD
8, 9103–9146, 2015

Algorithm 1 Inverse Modeling Approach

Input: time- and altitude-dependent emission domain $E = [t_0, t_f] \times \Omega$, total number and mass of SO_2 air parcels for the final forward simulation, meteorological data, satellite observations

1: Discretize the entire domain E, by considering n_t equal-sized intervals on the time axis and n_h heights along the altitude axis, respectively.

2: Distribute air parcels in all $N = n_t \cdot n_h$ subdomains of E uniformly. Set initial weights according to the equal probability strategy, $w_{ij} = 1/N$.

3: **Do**

4: Perform N unit simulations in parallel and calculate CSI time series.

5: Update importance weights w_{ij} based on one of the weight-updating schemes described in Sect. 3.3. Resample air parcels distributions according to importance weights.

6: **While** relative difference between adjacent importance weight matrices according to Eq. (5) is larger than a given tolerance.

7: Distribute air parcels in the entire initialization domain based on final importance weights.

8: Perform final forward simulation based on the reconstructed altitude-dependent time series of emissions.

Output: horizontal and vertical trace gas distributions (column densities, lists of air parcels) and diagnostic data (CSI plots) at different model time steps

GMDD
8, 9103–9146, 2015